Appl. Phys. A (2016) 122:376
DOI 10.1007/s00339-016-9869-1

Applied Physics A
Materials Science & Processing

Numerical study of near-, mid-, and long-infrared photon trapping in crystalline and amorphous HgCdTe metamaterials

Young Uk Jung[1] · Igor Bendoym[2] · David T. Crouse[1]

Received: 20 August 2015 / Accepted: 14 November 2015 / Published online: 14 March 2016

Abstract Recently, mercury cadmium telluride (HgCdTe) films have been extensively studied for the metamaterial applications. Crystalline HgCdTe (c-HgCdTe) films attracted people's attention for the spectral detection when used as metasurfaces and demonstrated reduced volume size, increased operating temperature, and improved quantum efficiency. Amorphous HgCdTe (a-HgCdTe) films also have been studied due to their interesting properties. Such properties include film deposition on any substrate, direct growth on device, and higher operating temperatures with the low dark current. Hence, in this work, for the first time, we investigate and compare the use of c-HgCdTe and a-HgCdTe for the photon sorting metasurfaces in near-, mid-, and long-IR spectral range in the sensor applications.

1 Introduction

Conventional HgCdTe sensors have "active" volume where the electron–hole pairs are generated within the semiconductor that is on the order of λ_r^3, where λ_r is the wavelength of operation of the device [1]. This large volume yields a high dark current. The c-HgCdTe-based infrared focal plane arrays (IRFPAs) also suffer from the thermal expansion mismatch between the Si readout integrated circuits (ROICs) and the detector components so that the format of IRFPAs is limited [2]. Thus, the "active" volume of the photodetectors has to be reduced, and the lattice mismatch issue has to be solved while keeping a high quantum efficiency (QE) [3].

In recent years, subwavelength plasmonic photon sorting devices that utilize metal–semiconductor–metal (MSM) posts [4] or localized surface plasmons (SPs) in multilayer semiconductors [5, 6] have been explored for the sensor applications. For example, Smith et al. [7] investigated reducing the absorber volume by etching a c-HgCdTe photonic crystal into the detector, allowing reduced dark current and improved noise-equivalent temperature difference. a-HgCdTe has also been gaining considerable attention not only because it solves the lattice mismatch issue but also because it utilizes the low-cost growth techniques such as sputtering or chemical vapor deposition (CVD), while the molecular beam epitaxy (MBE) technique or metal organic chemical vapor deposition (MOCVD) epitaxial systems have been used for the c-HgCdTe growth.

This paper numerically investigates and compares the use of c-HgCdTe and a-HgCdTe for the photon sorting metasurfaces. The proposed MSM designs collect and confine the radiation near the surface of c-HgCdTe and a-HgCdTe material and consequently reduce the thickness of the semiconducting layer to less than 0.5 μm, thereby also reducing the noise associated with high operating temperature (HOT) [8, 9].

2 Plasmonic resonators

The structure studied in this work for both c-HgCdTe and a-HgCdTe uses dispersion relation and propagation length of SP waves that are controlled by a periodic array of subwavelength metal–insulator–metal (MIM) or metal–

✉ Young Uk Jung
yj2198@gmail.com

[1] Department of Electrical Engineering, The City College of New York, New York, NY 10031, USA

[2] Phoebus Optoelectronics LLC, 419 Lafayette Street, New York, NY 10003, USA

semiconductor–metal (MSM) posts. On the metal–dielectric interface, the SP wave vector is given as $k_{sp} = k_o\sqrt{(\epsilon_m\epsilon_d)/(\epsilon_m + \epsilon_d)}$, where $k_o = \omega/c$, and ϵ_m and ϵ_d are the electric permittivities of the metal and dielectric materials, respectively [10]. The Drude model is used as it describes the frequency dependency of the metal:

$$\epsilon_m = \epsilon_m' + i\epsilon_m'' = \epsilon_\infty - \frac{\omega_p^2}{\omega(\omega + i\Gamma)}, \quad (1)$$

where ω_p is the plasma frequency and $\Gamma = e/(m_{eff}\mu_e)$ is the damping rate with e as the electron charge, and m_{eff} and μ_e as the effective mass and mobility of the charges, respectively. The initial dimensions of the structures can be chosen based on Fabry–Perot waveguide theory, where the cutoff frequencies ω_{mn} or wavelengths λ_{mn} are given by [11]:

$$\frac{\omega_{mn}}{c} = \frac{2\pi}{\lambda_{mn}} = \frac{\pi}{\sqrt{\epsilon}}\left(\frac{m^2}{\ell^2} + \frac{n^2}{w^2}\right)^{1/2}, \quad (2)$$

where ℓ is the length of the cavity, w is the width of the cavity, ϵ is the dielectric constant of the material filling the cavity, and m and n are integer numbers. Due to a Febry–Perot-like resonance of the guided mode, the MIM structure can exhibit a nearly total absorption at k_{sp}. Since the plasmonic resonators by MSM posts independently demonstrate spectral tunability, the combination of MSM resonators with different geometry on the metasurfaces can also independently sort the incident EM fields into the different spectral bands.

3 HgCdTe films

3.1 Crystalline HgCdTe films and amorphous HgCdTe films

The dielectric function of c-HgCdTe films changes depending on the cadmium (Cd) concentration and epitaxial growth of HgCdTe; hence, for our numerical calculation, we use the optical properties described by Norton et al. [12] and Liu et al. [13].

While optical, electronical, and structural properties of amorphous semiconductors have been extensively studied over the past few decades, a-HgCdTe has been investigated very recently [8, 14, 15]. For example, Wang et al. [16] reported, from his first-principle study, that the imaginary parts of dielectric function of a-HgCdTe show a large broad peak, which is in agreement with other amorphous semiconductors. While Wang et al. chose $x = 0.5$ where $Hg_{1-x}Cd_xTe$ to have random configuration, Jincheng et al. [3] used RF magnetron sputtering technique to deposit a-HgCdTe and experimentally measured the dielectric spectra of a-HgCdTe. The energy transition of a-HgCdTe was different from that of c-HgCdTe, i.e., whereas c-HgCdTe has many peaks and shoulders on its dielectric spectra between 1.7 and 4.7 eV, it is observed that a-HgCdTe has a single broad peak due to the disorder in the surface morphology. Feng et al. [8] found that the dark conductivity and photoconductivity of a-HgCdTe are different from those of c-HgCdTe. While the dark conductions (the dark conductivity and photoconductivity) of both c-HgCdTe and a-HgCdTe films increase with increasing temperature, the a-HgCdTe thin films show maximal photosensitivity at 240 K that is higher than that of polycrystalline thin films in the range from 170 to 300 K. Thus, these optical, electronical, and structural properties of a-HgCdTe have to be considered in the metamaterial designs as a-HgCdTe is utilized in the desired spectral range and operating temperature range.

In our work, we choose the dielectric function of a-HgCdTe by Kong et al. [17] for our numerical calculation, especially from 0.75 to 1.4 μm for the near-infrared spectral range. The optical data of a-HgCdTe given by [17] can be tuned with the amount of cadmium in the alloy composition and annealing temperature.

4 Modeling

Figure 1 shows a schematic of the polarization-independent 2D plasmonic metasurfaces that can be used for both c-HgCdTe and a-HgCdTe. This configuration allows for different ways of detecting the generated carriers in the HgCdTe semiconducting region: (1) The transparent and electrically conductive electrode such as indium tin oxide (ITO) can be deposited on top and can form a detector together with the bottom metal electrode, and (2) the interdigitated electrodes can be made as each metal unit cell is connected through a wire. The structure in Fig. 1 is the detector component that can be used as the focal plane array (FPA) and can be connected to the readout integrated circuits (ROICs). The effective index of the guided mode on the metasurfaces can be approximated as

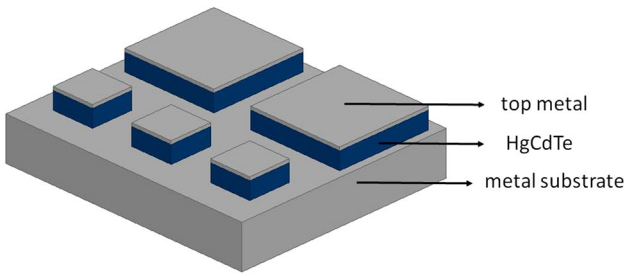

Fig. 1 A schematic of the polarization-independent 2D plasmonic metasurfaces that can be used for both c-HgCdTe and a-HgCdTe

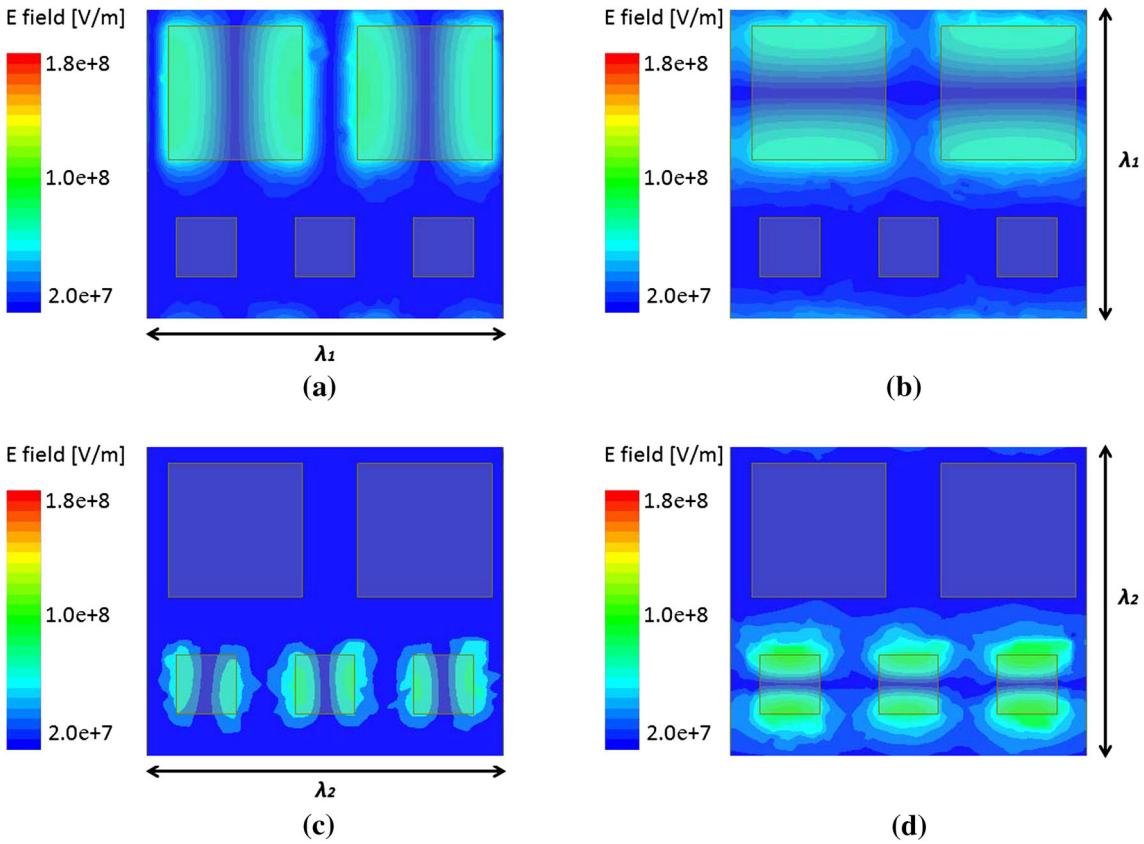

Fig. 2 Electric field distributions for the polarization-independent plasmonic device for mid-IR and long-IR dual responses using c-HgCdTe film. The light with two different wavelengths, λ_1 and λ_2, is incident. The *arrows* show the directions of the e-field polarization. One unit cell contains two kinds of MSM posts to maximize the fill factor [7]. The geometrical factor of the MSM posts can be adjusted for desired λ_1 and λ_2

$$n_{\text{eff}} + ik_{\text{eff}} = n_{\text{I}}\sqrt{1 + (i\lambda_{\text{sp}})/(\pi h_{\text{I}}\sqrt{\epsilon_{\text{metal}}})}, \tag{3}$$

where n_{I} is the index of the insulator and h_{I} is the thickness of the insulator [18]. Figure 1 will be used to build near-, mid-, and long-infrared plasmonic devices with different HgCdTe materials and different MSM geometrical parameters.

4.1 Mid- and long-IR plasmonic devices using c-HgCdTe

The analytic approach described by [19] is used to decide the size of the MSM posts and the periodicity. The finite element method (Ansys HFSS) is used to observe the plasmonic behaviors of the structure. While mid-wave infrared (MWIR) and long-wave infrared (LWIR) polarization-independent posts are shown, one can use a single type of resonator and the fill factor can be optimized by changing the number of each post for desired photon trapping.

To observe the surface plasmon fields, the real components of electric fields in the z-direction at each resonant frequency of LWIR and MWIR posts are calculated in Fig. 2. The period of the unit cell in the x-direction, Λ_x, is 2.6 μm, the period in the y-direction, Λ_y, is 3.5 μm, the thickness of HgCdTe layer, d_{MCT}, is 0.2 μm, and the thickness of gold layers on top of the HgCdTe posts, $d_{\text{top}_{\text{g}}\text{old}}$, is 20 nm while the thickness of gold substrate, $d_{\text{bottom}_{\text{g}}\text{old}}$, is 0.5 μm. The width of a smaller resonator, i.e., the MSM post for the MWIR spectral range, is $w_1 = 0.5$ μm, and a larger resonator, i.e., the MSM post for the LWIR spectral range, is $w_2 = 1.13$ μm.

The two different wavelengths, λ_1 and λ_2, indicate the resonant frequency of LWIR and MWIR, respectively. The arrows show the directions of the e-field polarization. One unit cell contains two kinds of MSM posts to maximize the fill factor [7]. The geometrical factor of the MSM posts can be adjusted for desired λ_1 and λ_2 in general [21]. Indium tin oxide (ITO) can be attached on the top of the MSM posts to serve as the conducting electrodes and collect the generated carriers in c-HgCdTe films. While the proposed design uses polarization-independent MSM posts, one can put polarization-dependent MWIR or LWIR posts and also adjust the fill factor.

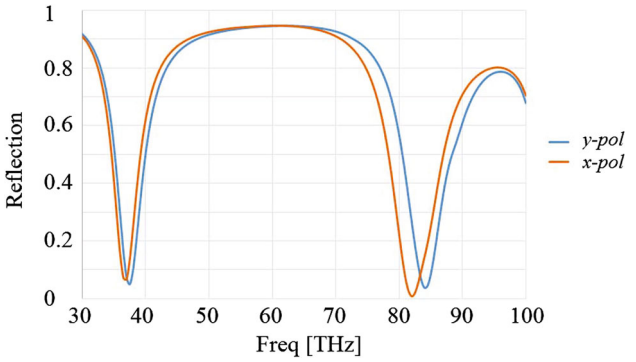

Fig. 3 Calculated reflections for mid-IR and long-IR dual response using c-HgCdTe films. The *blue line* is the reflectance when the e-field is polarized in the *y*-direction and the *orange line* is the reflectance when the e-field is polarized in the *y*-direction. Depending on the direction of the e-field polarization of the incident light, the resonant frequency is shifted

Figure 3 shows the numerically calculated dual-band reflectance by mid-IR and long-IR resonators. While the resonant frequency is slightly shifted depending on the direction of the e-field polarization, the filling factor [7] and the geometrical factor of the unit cell can be adjusted again for the desired λ_1 and λ_2.

4.2 Near-IR plasmonic device using a-HgCdTe

For near-IR plasmonic devices, a-HgCdTe material is used as c-HgCdTe material can be used for mid-to-mid IR spectral range. Figures 4 and 5 show the plasmonic and optical responses of the near-IR device. The semiconducting layer, i.e., a-HgCdTe film, is sandwiched by the top and bottom metal, compromising the metal–semiconductor–metal system. The thickness of a-HgCdTe, $t_{\mathrm{a-MCT}}$, can be approximately optimized when $t_{\mathrm{a-MCT}} = \lambda_r/(8n)$. The thickness of t_{gold} has almost no influence on the optical properties as soon as they are greater than the skin depth of the metal. Choosing the periodicity of 3/4 (λ_r/n) can avoid diffraction effects. Thus, to obtain the resonant frequency of 255 THz, we chose the periodicity, $\Lambda = 0.6$ μm and the thickness of a-HgCdTe, $t_{\mathrm{a-HgCdTe}} = 100$ nm. Notice that a-HgCdTe film at 255 THz (1.18 μm) still behaves as a semiconductor [3] so that this semiconducting region can be used for the photogeneration, where the QE can be exactly calculated by evaluating the normalized flux of the time-averaged Poynting vector along the interface of the metal pad.

The electric field distributions in Fig. 4a show that the photogeneration zone can be located below the top metal within the semiconducting region. Figure 4b shows the real components of the electric fields in the *z*-direction, i.e., the SP fields. This strong SP localization within the semiconducting region results in the maximum QE of 83 % as

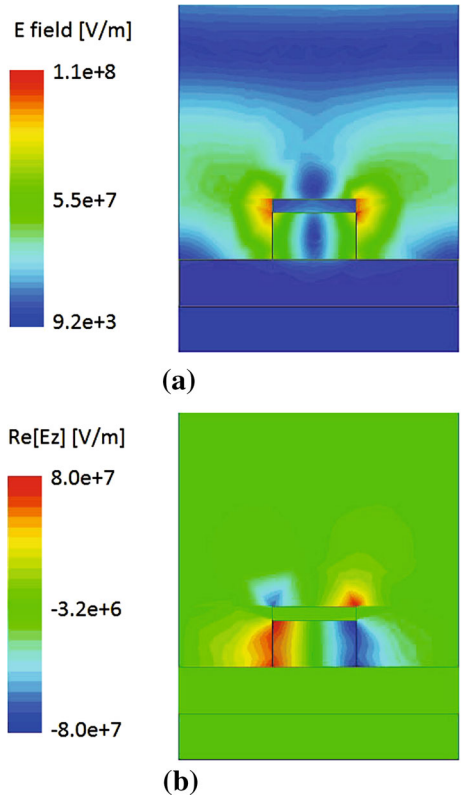

Fig. 4 **a** Simulated distributions of the electric fields using a-HgCdTe material in the near-infrared range at the resonant frequency of 255 THz. The periodicity, Λ, is 0.6 μm, and the thickness of a-HgCdTe, $t_{\mathrm{a-HgCdTe}}$, is 100 nm. Here, the thickness of the metal has almost no influence as long as it is greater than its skin depth. **b** The real components of electric fields in the *z*-direction show the decaying modes of subwavelength SPs

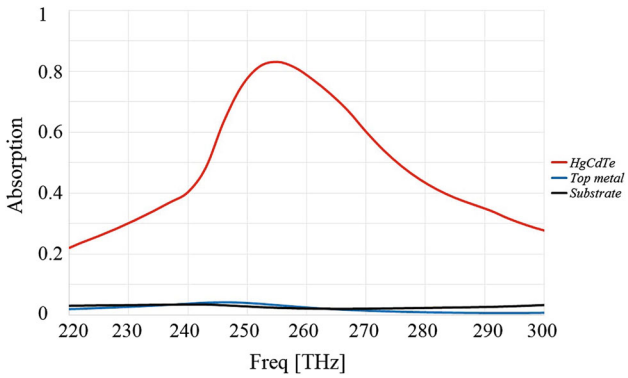

Fig. 5 Calculated absorption of the near-IR plasmonic device at 255 THz in Fig. 4. The maximum absorption of 83 % occurs at the resonant frequency inside the a-HgCdTe layer. Less than 5 % of little dissipation occurs for both the *top* metal and *bottom* metal

shown in Fig. 5. The resonant frequency in TM polarization, f_{TM}, is at 255 THz, and the resonant frequency in TE polarization, f_{TE}, is at 384 THz. In general, the 2D dot array has its resonant frequency located in the spectral

range between the resonant frequencies formed by TM and TE polarization.

Table 1 shows the calculated maximum absorption at each resonant frequency, i.e., near IR, mid-IR, and long IR, for a-HgCdTe and c-HgCdTe films. The maximum absorption or QE is calculated by evaluating normalized flux of the time-averaged Poynting vector along the given metasurfaces. Table 1 shows that photon trapping using both a-HgCdTe and c-HgCdTe films is possible with a proper choice of thin semiconducting layers.

Table 1 Comparison of maximum total absorption in metasurfaces for different detection wavelengths for c-HgCdTe and a-HgCdTe films in this work

	Near IR	Mid-IR	Long IR
Semiconducting layer	a-HgCdTe	c-HgCdTe	c-HgCdTe
Frequency	255 THz	82 THz	37 THz
Absorption in metasurfaces	88 %	98 %	93 %

The optical properties were taken from Refs. [12, 13, 17]

5 Discussion

While the effective optical properties of the metasurfaces can be approximated by Eq. (3), obtaining subwavelength SPs at even higher frequencies is challenging since the SP resonances also depend on the structural geometry such as filling vertical cavities. For example, Ourir et al. [20] showed the optical diffraction limit at visible and ultraviolet wavelengths as he proposed subwavelength far-field imaging system using a finite-sized ultrathin metallic slab. The plasmonic behaviors of the MSM configuration at 375 THz (0.8 μm), which is a higher frequency than 255 THz case in Fig. 4, are shown in Fig. 6. At a higher frequency, the gold has a negative permittivity with its absolute value decreasing and it also affects the wave propagation on the metal. The SP fields can be "leaking" outside the MSM configuration as shown in Fig. 6, where the periodicity, Λ is 0.2 μm and the thickness of a-HgCdTe, $t_{a-HgCdTe}$, is 38 nm. While the geometrical parameters are optimized to have the highest absorption possible, the absorption of a-HgCdTe film is 60 %, which is still lower than that of the maximum QE obtained at 255 THz.

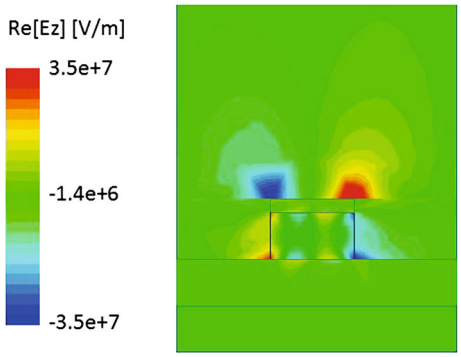

Fig. 6 SP field distributions at a higher frequency, 375 THz, using a-HgCdTe films. The metal becomes more lossy and transparent at this frequency that SP fields are leaking outside of the MSM configuration. Therefore, it lowers the QE compared to the previous system in Fig. 4. The dimension is optimized to obtain the best possible maximum QE of the system of 60 %: the periodicity, Λ, is 0.2 μm, and the thickness of a-HgCdTe, $t_{a-HgCdTe}$, is 38 nm

6 Conclusions

In this work, we investigated the use of metasurfaces for photon trapping in c-HgCdTe and a-HgCdTe films that confines the light inside the MSM configuration and consequently reduces the thickness of the semiconducting layer, which yields a lower dark current. The use of a-HgCdTe films to make the photon sorting metasurfaces also has benefits that cannot be found from c-HgCdTe films, e.g., a-HgCdTe film can be grown on any materials [3, 8], and the growth of a-HgCdTe film on Si surface is desirable for Si readout integrated circuits (ROICs). Si-based a-HgCdTe IR photoconductive detector can also operate at 80–300 K [16]. Thus, we numerically studied both c-HgCdTe and a-HgCdTe films for photon trapping metasurfaces. One has to carefully consider the optical gap in the spectral range where the absorption coefficient becomes stable. As a-HgCdTe film is combined with metal, the plasmonic behaviors have to be checked accordingly to maximize the QE in the desired spectral range, and thereby lower the dark current coming from the active volume and increase the operating temperature.

Acknowledgments This work was supported by the NSF Industry University Cooperative Research Center for Metamaterials (IIP-1068028).

References

1. J. Le Perchec, Y. Desieres, R.E. de Lamaestre, Plasmon-based photosensors comprising a very thin semiconducting region. Appl. Phys. Lett. **94**, 181104 (2009)
2. J. Wang, X. Chen, W. Hu, L. Wang, W. Lu, F. Xu, J. Zhao, Y. Shi, R. Ji, Amorphous HgCdTe infrared photoconductive detector with high detectivity above 200 K. Appl. Phys. Lett. **99**, 113508 (2011)
3. W. Guanghua, K. Jincheng, L. Xiongjun, Q. Feng, L. Cong, Y. Lili, K. Lingde, J. Rongbin, Effect of power variation on microstructure and surface morphology of HgCdTe films

deposited by RF magnetron sputtering. J. Semicond. **31**(5), 053004–053005 (2010)
4. J. Hao, L. Zhou, M. Qiu, Nearly total absorption of light and heat generation by plasmonic metamaterials. Phys. Rev. B **83**, 165107 (2011)
5. I.M. Mandel, I. Bendoym, Y. Jung, A.B. Golovin, D.T. Crouse, Dispersion engineering of surface plasmons. Opt. Express **21**, 31883–31893 (2013)
6. Y. Jung, I.M. Mandel, I. Bendoym, A.B. Golovin, D.T. Crouse, Surface plasmon sorting and engineered dispersion curves using multilayer doped semiconductors. J. Opt. Soc. Am. B **32**, 1007–1012 (2015)
7. K.D. Smith, J.G.A. Wehner, R.W. Graham, J.E. Randolph, A.M. Ramirez, G.M. Venzor, K. Olsson, M.F. Vilela, E.P.G. Smith, High operating temperature mid-wavelength infrared HgCdTe photon trapping focal plane arrays. Proc. SPIE **8353**, 83532R (2012)
8. Q. Feng, X. Jinzhong, K. Jincheng, Y. Lianjie, K. Lingde, W. Guanghua, L. Xiongjun, Y. Lili, L. Cong, J. Rongbin, Dark conductivity and photoconductivity of amorphous $Hg_{0.78}Cd_{0.22}Te$ thin film. J. Semicond. **32**, 033004 (2011)
9. Y. Jung, I. Bendoym, A.B. Golovin, D.T. Crouse, Dual-band photon sorting plasmonic MIM metamaterial sensor. Proc. SPIE **9070**, 90702X (2014)
10. H. Raether, *Surface Plasmons on Smooth and Rough Surfaces and On Gratings, Vol. 111 of Springer Tracts in Modern Physics* (Springer, Berlin, 1988)
11. J. Jackson, *Classical Electrodynamics* (Wiley, London, 1975)
12. P. Norton, HgCdTe infrared detectors. Opto-Electron. Rev. **10**(3), 159–174 (2002)
13. K. Liu, J.H. Chu, D.Y. Tang, Composition and temperature dependence of the refractive index in $Hg_{1-x}Cd_xTe$. J. Appl. Phys. **75**, 4176 (1994)
14. J.D. Joannopoulos, M.L. Cohen, Electronic properties of complex crystalline and amorphous phases of Ge and Si. II. Band structure and optical properties. Phys. Rev. B **8**, 2733 (1973)
15. S. Adachi, H. Mori, Optical properties of fully amorphous silicon. Phys. Rev. B **62**, 10158 (2000)
16. L. Wang, X. Chen, W. Lu, Y. Huang, X. Wang and J. Zhao, Optical property of amorphous semiconductor mercury cadmium telluride from first-principles study. Sci. China Ser. E-Technol. Sci. **52**(7), 1928–1932 (2009)
17. J.C. Kong, S.L. Wang, L.D. Kong, J. Zhao, Y. Ma, G.H. Wang, X.J. Li, L.L. Yang, P.J. Zhang, R.B. Ji, Studies of RF magnetron sputtered amorphous HgCdTe films. Proc. SPIE **7383**, 73833Y (2009)
18. S. Collin, F. Pardo, J. Pelouard, Waveguiding in nanoscale metallic apertures. Opt. Express **15**, 4310–4320 (2007)
19. J. Le Perchec, P. Quemerais, A. Barbara, On light addressing within subwavelength metallic gratings. J. Lightwave Technol. **26**, 638 (2008)
20. A. Ourir, M. Fink, Subwavelength far-field imaging at visible and ultraviolet wavelengths using broadband surface plasmon waves. Phys. Rev. B **89**, 115403 (2014)
21. Y. Jung, M. Liu, I. Bendoym, A.B. Golovin, D.T. Crouse, Wavelength selective surface plasmons enhanced infrared photodetectors. In *Systems, Applications and Technology Conference (LISAT), 2014 IEEE Long Island*, pp. 1–6 (2014)